Hierarchy of multi-order skyrmion phases in twisted magnetic bilayers

Sujay Ray and Tanmoy Das*
Department of Physics, Indian Institute of Science, Bangalore 560012, India

(Received 29 January 2021; revised 12 May 2021; accepted 15 June 2021; published 8 July 2021)

The recent discovery of two-dimensional (2D) van der Waals magnets is a crucial turning point in the quantum magnet research field, since quantum fluctuations and experimental difficulties often elude stable magnetic orders in two dimensions. This opens new doors to delve for novel quantum and topological spin configurations, which may or may not have direct analogs in bulk counterparts. Here we study a twisted bilayer geometry of 2D magnets in which long-range spin-spin interactions naturally commence along the interlayer Heisenberg ($J_\perp$) and dipole-dipole (J_D) channels. The $J_\perp$-J_D parameter space unveils a hierarchy of distinct skyrmion phases, including point-, rod-, and ring-shaped topological charge distributions. Furthermore, we predict a topological antiferroelectric phase, where oppositely charged antiskyrmion pairs are formed, and the corresponding topological dipole moments become ordered in a Néel-like state—hence dubbed the topological antiferroelectric state. The results indicate that the twisted magnetic layer provides a versatile setting to engineer and tune a plethora of skyrmion phases and their dynamics.

DOI: 10.1103/PhysRevB.104.014410

I. INTRODUCTION

A skyrmion is a particle dual to a topological configuration of the $O(3)$ fields (read spin) in a 2+1 dimension [1–4]. Such a spin configuration is an allowed classical solution of the nonlinear sigma model. However, the main challenge lies in stabilizing a skyrmion solution at a saddle-point energy minimum, requiring distinct magnetic interactions and frustration. Long-range dipole-dipole interaction, in addition to easy-plane magnetic anisotropy and magnetic field, was initially proposed to mediate skyrmion solution [5]. The Dzyaloshinskii-Moriya interaction (DMI) brings in the chiral spin-spin interaction required for a skyrmion solution [2,6–9]. Competition between DMI and ferromagnetic exchange interactions makes a spatially varying magnetic texture have a lower energy than the mean-field long-range magnetic order. Geometrical and magnetic frustration can also stabilize skyrmion structures [10–13]. This is induced, for example, in a triangular lattice by the competition between a ferromagnetic nearest-neighbor exchange with an antiferromagnetic next-nearest-neighbor interaction. Apart from these, more recently, spin-orbit coupling (SOC) [14], Kondo coupling [15], and magnetic disorder with the application of magnetic pulse [16] are shown to assist skyrmion solution. Proposals to obtain skyrmions via quantum Hall substrates [17] and optical lattices [18] are also presented.

By now, there have been several material realizations of the skyrmions, mainly in systems with DMI, such as Bloch-type skyrmions in MnSi [19], $Co_{0.5}Fe_{0.5}Si$ [20–22], Cu_2OSeO_3 [23], CoZnMn [24], and FeGe [25], and Néel-type skyrmions in ferromagnetic heavy metals [26], Kagome lattice Fe_3Sn_2 [27], magnetic films [28], and antiskyrmions in Mn_2RhSn [29,30]. Experimental abilities to breed [22,31], mobilize [32], and rotate [33] skyrmions have been also demonstrated recently [28,34]. Owing to topological robustness, skyrmions have numerous potential applications in quantum information [35] and racetrack memory [36,37], which demand enhanced material flexibilities and tunabilities.

Obtaining skyrmion solutions in two-dimensional (2D) systems will give new opportunities for science and applications. Recently, long-range magnetic order has been observed in 2D van der Waals (VDW) chalcogenides, halides, and related materials. Intrinsic antiferromagnetic order is observed in monolayer $FePS_3$ [38,39], and in MPX_3(M = Mn, Fe, Co, Ni; X = S, Se) [40,41]. Later on, many VDW materials such as Fe_3GeTe_2 [42,43], MnX_2(X = S, Se) [44,45], and VX_2(X = S, Se, Te) [46–48] were found to be intrinsic ferromagnets. Another exciting family of 2D VDW magnets is the Cr based materials CrX_3 (X = I, Br, Cl) [49,50], which are ferromagnets in monolayer, but antiferromagnets in bilayer structure, and the two orderings are externally tunable [51,52]. Theoretical and experimental efforts to obtain skyrmions in 2D systems are present. Continuum theory of magnetization fields in the nonlinear sigma model and Landau-Lifshitz-Gilbert model in monolayer and bilayer moiré systems show the existence of Neél type skyrmions [53–57]. Recently, a skyrmion phase was observed in 2D Fe_3GeTe_2 on the $(Co/Pd)_n$ superlattice [58] and Fe_3GeTe_2/h-BN heterostructure [59] due to their sizable DMI strength.

To strategize a new mechanism of the skyrmion, it is worth revisiting its key ingredients. First, topological skyrmion configurations in 2+1 dimension generally belong to the homotopy group $\pi_2(\mathbb{S}^2) \cong \mathbb{Z}$. The homotopy mapping is exact when both the coordinate space and the target (spin) space are compact $\mathbb{S}^2$. The constraint $|\mathbf{S}| = 1$ compactifies the spin

*tnmydas@iisc.ac.in

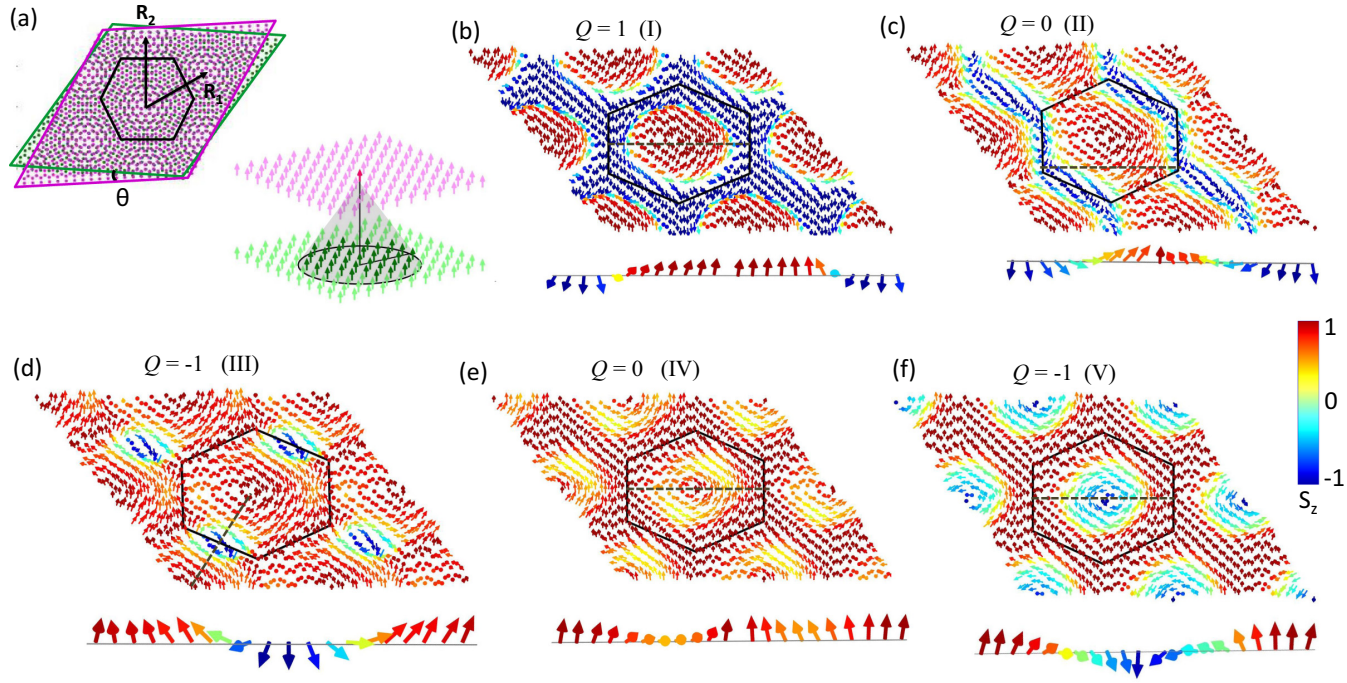

FIG. 1. Twisted bilayer setup and five distinct topological spin configurations in real space. (a) Schematic diagram of a twisted bilayer honeycomb (θ = twist angle) lattice with a moiré pattern shown along with two lattice translation vectors $\mathbf{R}_{1,2}$. A 3D illustration is shown in the lower right corner, in which a single spin of the upper layer (bright magenta color) interacts with bottom-layer spins within a circular region (dark green color) of radius r_{cut}. (b)–(f) Five distinct spin textures (enumerated by phase I to phase V, see Fig. 5 for zoomed view) obtained in the $J_\perp$-J_D parameter space (see Fig. 2). Arrows denote the spin **s** vector, while the red to green color gradient denotes $s_z = 1$ to -1 values. The dashed thin line in each panel indicates the direction along which a 2D spin projection is shown in the corresponding inset. (b), (d), (f) Three skyrmion structures with distinct charge density (shown in Fig. 3) and integer topological charge Q. (c) Phase II corresponds to a higher-order topological phase with streamlines of down spins, and topological dipole moments of antiskyrmions pairs (see Fig. 4). (e) A trivial topological phase with finite noncollinear ferromagnetic moment.

space. When a spin configuration has a one-to-one correspondence with the spatial dimensions, this in turn compactifies the position space $\mathbb{R}^2 \to \mathbb{S}^2$. The resulting one-to-one mapping guarantees the spin configuration to be topological with its skyrmion charge $Q \in \mathbb{Z}$—an integer winding number. We can reverse the above reasoning for a bottom-up approach. If the effective magnetic field $\mathbf{B}(\mathbf{r})$, experienced by a local spin due to the surrounding spins and extrinsic fields, lives on a Bloch sphere $\mathbb{S}^2$, then within the minimal Zeeman-like coupling, the field would lay the ground for a topological configuration for the spins. The second essential requirement is that the local field configuration must concomitantly promote a saddle-point energy minimum to stabilize a skyrmion structure.

Guided by these principles, and with the recent discoveries of 2D magnets, we lay a blueprint for multifaceted skyrmions (and antiskyrmions) in twisted magnetic bilayers. We construct a moiré superlattice of spins formed in a twisted bilayer of VDW magnetic layers with ferromagnetic order at the bottom and $O(3)$ spin dynamics on the top layer. The setup is illustrated in Fig. 1(a). We include Heisenberg exchange terms $J_{||}$ (for intralayer) and $J_\perp$ (for interlayer) interactions, and the interlayer dipole interaction J_D as shown in density functional theory (DFT) calculations to be dominant in such a setup [53]. We carry out Monte Carlo simulations to determine the microscopic ground state spin configurations at low temperature, and sweep the entire $J_\perp/J_{||}$ and $J_D/J_{||}$ parameter space. We identify three distinct skyrmion phases with topological charges $Q = \pm 1$, the topological charge distributions of which reveal a previously unknown hierarchy of point, rod, and ring shapes in different topological phases. We predict a distinct topological spin configuration in the vicinity of $J_\perp/J_D \sim -0.4$. We find that near the moiré lattice sites, a pair of spatially separated and oppositely charged antiskyrmions is formed and governs a topological ("electric") dipole moment. More interestingly, such dipoles are found to align antiferroelectrically between the nearest-neighbor sites of the moiré lattice, and produce a Néel-like order for the topological electric dipole moment. We explain these results with a dual electromagnetic theory, demonstrating the "electric field" lines for all topological charge distributions. We also study the "x-ray-diffraction" (XRD) pattern of the topological charges (topological charge-charge correlation function) as well as the spin-spin correlation functions to elucidate the crystallization and phase transitions of the topological charge centers and dipoles. These results expand the list of possible skyrmion and magnetic phases (Néel and Bloch phase) obtained in continuum models to a hierarchy of skyrmions and its higher-order topological phase [54,60].

II. REALIZATION

We consider a single layer honeycomb magnet (magenta color) placed on a single layer magnetic substrate (green

color) of the same lattice structure and lattice constant, as shown in Fig. 1(a). The distance between the layers d is taken to be the same as the lattice constant of the honeycomb lattice. The spin in the substrate layer is fixed to be a collinear ferromagnetic state. This can be achieved with a strong bulk ferromagnetic material as studied in the literature [56]. We primarily focus on small relative twist angles θ which give the commensurate moiré superlattices. We focus on $\theta = 1.61^\circ$, which gives a hexagonal moiré lattice with $a = 35.6a_0$, where a_0 is the lattice constant of the single layer system. A critical number of atoms in a moiré supercell, determined by the twist angle, is important to stabilize a skyrmion. Above this critical value, the obtained topological phase diagram remains essentially invariant to twist angles and number of atoms, except that the skyrmion radius grows with the moiré cell dimension. So, there is an upper critical value of the twist angle ($\approx 2^\circ$) above which the moiré unit cell becomes small enough and the magnetic unit cell is no longer commensurate with the moiré unit cell.

The general computational strategy is as follows. We split the full Hamiltonian into two parts: $H = H_1 + H_2$, where H_1 and H_2 are the intralayer and interlayer parts. The intralayer Hamiltonian consists of a nearest-neighbor Heisenberg exchange and a spin asymmetry term, for both layers. The interlayer term consists of a many neighbors Heisenberg exchange term and the dipole-dipole interaction term. We then integrate out the bottom layer's spin to obtain an effective Hamiltonian for the top layer as $H_{\text{top}} \sim H_1 + \mathbf{B}\cdot\mathbf{s}$, where $\mathbf{B}$ is the effective magnetic field exerted from the bottom layer on the top layer spin $\mathbf{s}$. The moiré periodicity is imposed by expanding these terms in the plane wave basis of the moiré supercell. We solve H_{top} within the Monte Carlo simulation.

We now give the details of the model. We label the spin variables for the top and bottom (substrate) layers by $\mathbf{s}$ and $\mathbf{S}$, respectively. The 2D VDW systems in single and bilayer setups are observed to show an in-plane ferromagnetic (and out-of-plane ferromagnetic or antiferromagnetic) order with the spin quantization axis to be out of plane (z direction) [61,62]. Such a magnetic ground state is reproduced by the model

$$H_1(\mathbf{s}) = -J_{||}\sum_{<ij>}\mathbf{s}_i.\mathbf{s}_j - K\sum_i (s_{iz})^2, \tag{1}$$

where i and j are lattice sites within a moiré supercell. The first term is the nearest-neighbor Heisenberg interaction with coupling constant $J_{||} > 0$ for a ferromagnetic phase, and K gives the z-axis asymmetry, breaking the $O(3)$ spin degeneracy. $H_1(\mathbf{S})$ gives the corresponding Hamiltonian for the bottom layer, with $J_{||}$ and K kept fixed.

The interlayer interaction H_2 is the crucial part. Depending on the twist angle, especially at small twist angles, a spin at the top layer interacts with several neighboring bottom layer spins, and hence the interlayer interaction involves terms beyond the nearest-neighbor exchange interaction. The interlayer interaction is mainly dominated by several nearest-neighbor exchange interactions H_{ex} and dipole-dipole interactions (H_D) as $H_2(\mathbf{S},\mathbf{s}) = H_{\text{ex}} + H_D$ where

$$H_{\text{ex}} = -\sum_{ij} J_\perp(\mathbf{r}_{ij})\mathbf{S}_i.\mathbf{s}_j, \tag{2}$$

$$H_D = J_D\sum_{ij}\frac{1}{r_{ij}^3}[\mathbf{S}_i.\mathbf{s}_j - 3(\mathbf{S}_i.\hat{\mathbf{r}}_{ij}).(\mathbf{s}_j.\hat{\mathbf{r}}_{ij})]. \tag{3}$$

i and j are the site indices in the bottom and top layer, respectively. $\mathbf{r}_{ij} = \mathbf{r}_i - \mathbf{r}_j$ with $\hat{\mathbf{r}}_{ij}$ being the corresponding unit vector. Since both interactions are long ranged, we need to set a cutoff radius r_{cut}, Fig. 1(a) (inset). Due to higher power of r_{ij} in the denominator, the result converges quickly by $r_{\text{cut}} < 20a_0$ which is much smaller than the moiré lattice size $\approx 35a_0$.

Next, we integrate out the bottom layer's spins $\mathbf{S}$, and define an effective magnetic field at the top layer at $\mathbf{r}_i$ as $\mathbf{B}(\mathbf{r}_i) = \mathbf{B}_{\text{ex}}(\mathbf{r}_i) + \mathbf{B}_D(\mathbf{r}_i)$, where $\mathbf{B}_{\text{ex}}$ and $\mathbf{B}_D$ distinguish the contributions from the exchange and dipole-dipole interaction terms as $\mathbf{B}_{\text{ex}}(\mathbf{r}_i) = -\frac{\partial H_{\text{ex}}}{\partial \mathbf{s}_i} = \frac{J_\perp}{2}\sum_a e^{i\mathbf{G}_a.\mathbf{r}_i}$ and $\mathbf{B}_D(\mathbf{r}_i) = -\frac{\partial H_D}{\partial \mathbf{s}_i}$.

We set $\mathbf{S}_j = \hat{z}$ for all unit spins at the bottom layer. $\mathbf{G}_a (a = 1\text{–}6)$ are the six minimal reciprocal lattice vectors of the moiré superlattice. We include the six possible smallest reciprocal lattice vectors in the moiré lattice and the results do not change with the inclusion of negligibly small contribution of higher reciprocal lattice vectors. Dipole interaction is known to be a useful ingredient for (generally bubble-type) skyrmions and antiskyrmions [3,5,30], but is significantly weaker in strength in real materials. In a twisted bilayer system, however, the interlayer dipole interaction is considerably enhanced, and is found here to be detrimental to the bubble or Bloch skyrmion phases (see below), while promoting distinct skyrmion phases.

In this algorithm, the bottom layer's effects can be cast into a Zeeman-like term at the top layer. The full Hamiltonian hence takes the form

$$H = H_1 - \sum_i \mathbf{B}(\mathbf{r}_i)\cdot\mathbf{s}_i. \tag{4}$$

In this way, the total Hamiltonian simplifies to the form used in the introduction for discussing how the in-plane spin is enforced to lie on a topological compact space $\mathbb{S}^2$ by tailoring the "long-range" Zeeman coupling.

In our Monte Carlo simulation we minimize the local Hamiltonian for a single spin with temperature annealing as well as parameter annealing, and check for the total energy convergence of the system in each case. In all our calculations, the minimization of the local Hamiltonian corresponds to minimization of the total energy. Details of our Monte Carlo simulation can be found in Appendix B.

Our model and parameters are justified as follows. Note that the dipole-dipole interaction J_{D} is only included in the interlayer Hamiltonian. This is because, in VDW magnets, DFT calculation has indicated that the intralayer exchange is almost ten times larger than the interlayer exchange [53]. Therefore, any small amount of interlayer dipole-dipole interaction can have considerable effect on the spin configuration, whereas the intralayer dipole interaction is always subsided by the large exchange interaction. Furthermore, the DMI in the existing 2D VDW magnets is small compared to strong

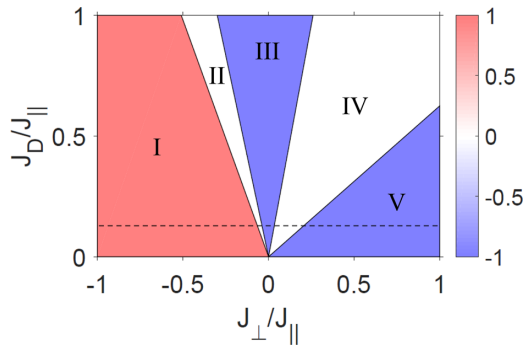

FIG. 2. Phase diagram of five distinct topological and quantum phases. The interlayer exchange coupling $J_\perp$ and dipole interaction J_D are varied with respect to the in-plane exchange coupling $J_{||}$. $J_D < 0$ is an unphysical value; however, mathematically it leaves the phase diagram symmetric when the sign of $J_\perp$ is also reversed. Red and blue color distinguishes skyrmion charges of $Q = \pm 1$. Phase II, although it features a net $Q = 0$, exhibits a topological dipole moment of antiskyrmions which produces an antiferroelectric order state. The horizontal dashed line indicates the realistic parameter range as deduced in a DFT calculation [53].

intralayer exchange interaction. Therefore, realistic small values of the intralayer dipole interaction and DMI interaction do not impact our phase diagram (see Discussion section). The realistic parameter range in CrI_3 is indicated by the horizontal dashed line in Fig. 2, as deduced from a DFT calculation [53]. Interestingly, the phase diagram essentially remains the same below and above this parameter range, emphasizing that all the phases are attainable in the existing materials.

III. RESULTS

A. Phase diagram

Our simulation yields a plethora of quantum and topological phases; five such distinct configurations are identified in Figs. 1(b)–1(f). We do not however find any homogeneous mean-field solutions at finite twist angles, while at zero twist angles we only find either a ferromagnetic or an antiferromagnetic order depending on the sign of $J_{||}$. The corresponding phase diagram is presented in Fig. 2 for $J_\perp/J_{||}$ and $J_D/J_{||}$ with $J_{||} > 0$. In the phase diagram, the red and blue shaded areas denote distinct skyrmion phases with topological invariant $Q = \pm 1$, respectively. The white regions represent a higher-order dipolar antiskyrmion phase (phase II), and a trivial phase (phase IV). From Figs. 1(b), 1(d), and 1(f), it is evident that the three skyrmion phases, denoted by phase I, III, and V, are characteristically exclusive, which will be distinguished below in multiple ways. Phase II has zero net topological charge, but possesses fractional charge centers of opposite sign, and hence a topological dipole moment which is antiferroelectrically ordered. Phase IV bears no topological or exotic quantum order (except a finite magnetization due to a collinear spin ordering).

The particle dual of the skyrmion is a topological charge denoted by $Q = \int d^2\mathbf{r}\rho(\mathbf{r})$, where $\rho(\mathbf{r})$ is the topological charge density. With its corresponding current density $\mathcal{J}_{x,y}$, we concisely define the three-component density operators $\mathcal{J}_\mu = (\rho, \mathcal{J}_x, \mathcal{J}_y)$ as

$$\mathcal{J}_\mu(\mathbf{r}) = \frac{\epsilon_{\mu\nu\tau}}{8\pi}\mathbf{n}\cdot\partial_\nu\mathbf{n}\times\partial_\tau\mathbf{n}, \tag{5}$$

where $\mu, \nu, \tau = 0, x, y$ are time-space indices, and the $\mathbf{r}$ dependence on the unit vector field $\mathbf{n} = \mathbf{s}/|\mathbf{s}|$ is implied. We define the vortex density as $\mathbf{v}(\mathbf{r}) = \epsilon_{\nu\tau}\partial_\nu\mathbf{n}\times\partial_\tau\mathbf{n}$. In our layered geometry and with the z-axis asymmetry, it is natural to expect that the vorticity of the spin texture commences in the xy plane, i.e., v_z dominates. Then the corresponding polarity density is simply governed by $n_z(\mathbf{r})$. The z components of the polarity density $n_z(\mathbf{r})$, the vortex density $v_z(\mathbf{r})$, and the charge density $\rho(\mathbf{r})$ are illustrated in Fig. 3 in three different rows for the five distinct phases (different columns).

The mechanism of skyrmions and antiskyrmions is retrieved as follows. It is known from the topological band theory [63] that the polarity field (equivalent to the Dirac mass for fermion fields) forms a nodal (closed) contour, across which $n_z(\mathbf{r})$ changes sign—this is called the domain wall (see top row in Fig. 3). The vorticity field $v_z(\mathbf{r})$ inside the domain wall acquires singularity—either point-, rod-, or ring-shaped singularity—and cannot be removed with a trivial gauge transformation (see middle row in Fig. 3). Hence the topological charge density $\rho(\mathbf{r})$ becomes confined within the domain wall (see bottom row in Fig. 3). The homotopy mapping of the $\mathbf{n}(\mathbf{r})$ field on $\mathbb{S}^2$ in the $\mathbf{r}$ space quantizes the topological charge $Q \in \mathbb{Z}$, where the integration of $\mathbf{r}$ is performed within a single domain wall of the polarity density [see black solid lines in Figs. 3(f)–3(o)].

B. Skyrmion hierarchy

Phase I is a topological phase with $Q = -1$, and is present in most of the $J_\perp/J_{||} < 0$ region. It is destabilized at a small value of $J_\perp$ by stronger dipole interaction J_D. The distributions of n_z, v_z, and ρ for phase I are shown in the leftmost column in Fig. 3. The polarity density map $n_z(\mathbf{r})$ demarcates a sharp and circular domain wall boundary, which reminds us of a magnetic bubble observed in astronomical space, as well as in magnetic systems [64]. The vorticity and charge densities of this phase, however, reveal much richer structures unknown before. In Fig. 3(f), we find that the nodal ring of the polarity density (black line) encloses a circular vortex density $v_z(\mathbf{r})$ structure. In fact, $v_z(\mathbf{r})$ is positive (negative) outside (inside) the domain wall, and shares the same nodal ring as that of $n_z(\mathbf{r})$. In what follows, the charge density $\rho(\mathbf{r})$ also acquires a singular ring geometry, confined by the domain wall boundary [see Fig. 3(k)]. This phase is also topologically equivalent to the Dirac nodal ring state [65] in the electronic structure in which the topology is defined via Berry gauge connection.

As we switch $J_\perp \to -J_\perp$, keeping all other interactions fixed, we obtain a characteristically distinct skyrmion texture (denoted by phase V) with opposite charge Q. Unlike the sharp domain wall in phase I, n_z varies smoothly with $\mathbf{r}$, and forms a (nearly) elliptical domain wall in phase V. Moreover, the phase V has a pointlike topological charge center sitting at the moiré supercell center. Hence as opposed to ring singularity in phase I, phase V acquires point singularity. The asymmetry between phase I and phase V at $\pm J_\perp$ for fixed J_D

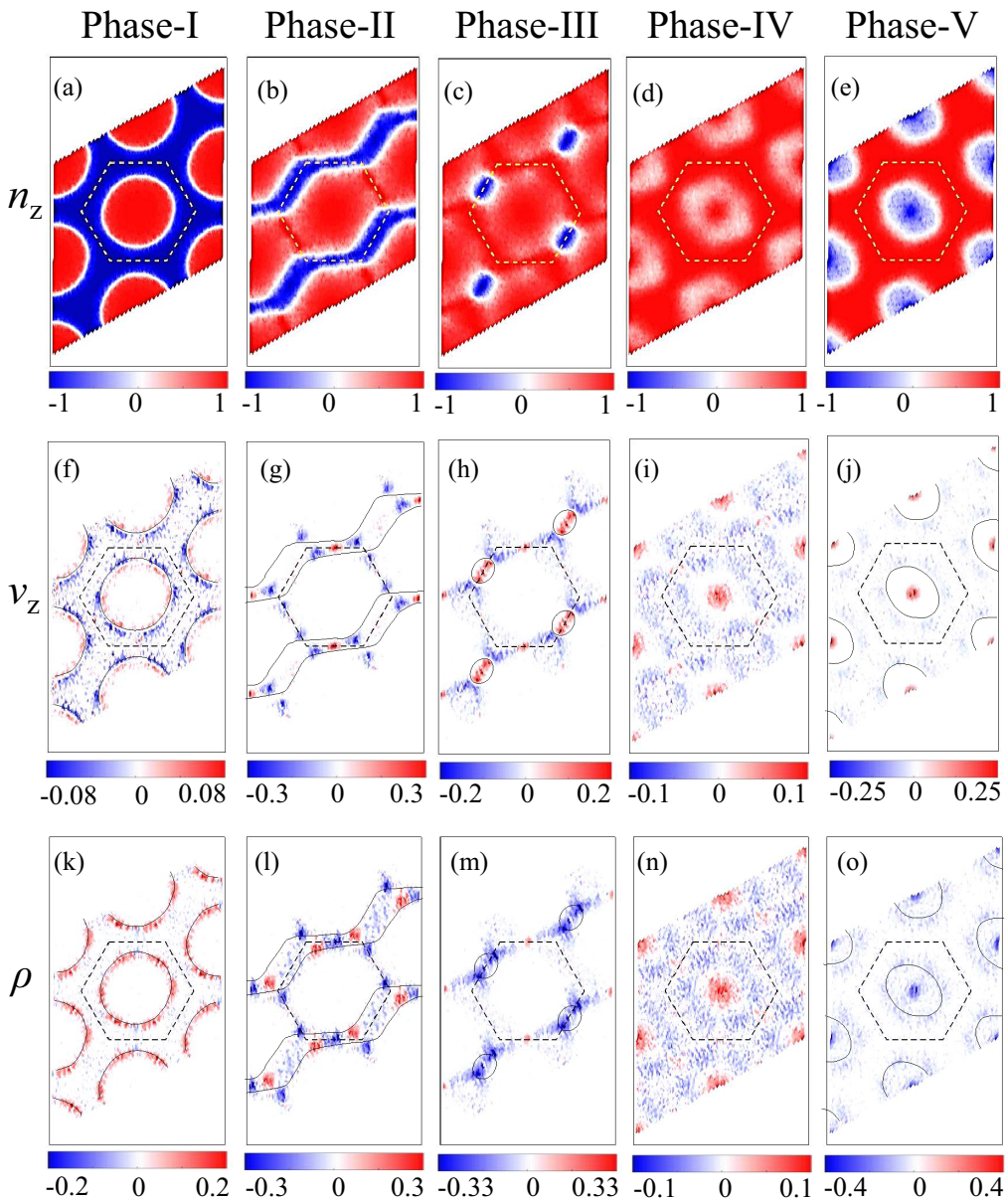

FIG. 3. Local variation of polarity, vorticity, and topological charge densities in the five different topological phases. (a–e) The z component of the polarity density $n_z(\mathbf{r})$ (see main text) is plotted in a blue to red color map, denoting down- to up-spin components of s_z. (f–j) We plot the vorticity density $v_z(\mathbf{r})$ with a blue to red color map. The black solid line marks the $n_z = 0$ domain wall boundary. (k–o) Corresponding topological charge density $\rho(\mathbf{r})$. In phase II and IV, although charge centers are formed, the net charge $Q = 0$. In phase II, fractional charge centers are confined by the streamline domain wall, giving a topological dipole moment. There is no domain wall of n_z in phase IV and hence it is a trivial phase. (Different color scales are for the five phases in the middle and bottom panels.)

results from the competition between $J_\perp$ and J_D. The phase diagram is reversal between $\pm J_\perp$ for $J_D \to -J_D$.

The skyrmion phase III occurs in the vicinity of $J_\perp \sim 0$, and is mainly stabilized by the long-range (out-of-plane) dipole-dipole interaction J_D. The magnetic domains are elliptical in shape, and concentrated at two sides of the moiré supercell. As seen in Figs. 3(h) and 3(m), the n_z nodal contour confines a fixed-sign vorticity field (positive), and hence the topological charge distribution (negative since $n_z < 0$) becomes quantized. The topological charge density is distributed inside the elliptical domain wall and gives a rodlike singularity. Such a rodlike topological charge distribution repeats periodically [see Fig. 3(m)] and gives a nematic or smectic crystal.

In all three skyrmion phases, each moiré supercell contains a single skyrmion configuration. Therefore, a suitable characteristic length scale associated with different skyrmions can be defined by the domain wall contour $\mathbf{r}_\mathrm{d}$ where $n_z(\mathbf{r}_\mathrm{d}) = 0$. This condition is very much satisfied where the effective magnetic field due to the bottom layer along the z direction vanishes, i.e., $B^z_{\mathrm{ex}}(\mathbf{r}_\mathrm{d}) + B^z_D(\mathbf{r_d}) = 0$. From the expression for B_{ex} and $B_\mathbf{D}$ given in Appendix A, we see that $\mathbf{r}_\mathrm{d}$ depends on the ratio $J_\perp/J_D$, and the interlayer distance d for a given moiré lattice. Depending on the ratio $J_\perp/J_D$, the condition can turn

into an equation of a circle or an ellipse, as we also find numerically. In phase III, the domain wall takes an elliptic shape in Fig. 3(h) and the two topological charge centers we find here in Fig. 3(m) sit at the two focal points.

It is then easy to grasp that a skyrmion phase transition occurs when domain wall radius $\mathbf{r_d}$ either shrinks to zero or expands to the moiré cell boundary $\mathbf{R}_{1,2}$. The phase transition between phase I and phase II occurs when $\mathbf{r}_d = \mathbf{R}_1$ or $\mathbf{R}_2$. The rotational symmetry breaking renders a small domain wall to form in phase III with opposite polarity at one of the moiré supercell's site for small values of $J_\perp$, as seen in Fig. 3(c). This small domain wall then shrinks to zero with the sign reversal of $J_\perp$ which disfavors the domain wall of negative polarity. Curiously, there still exists a finite vortex structure and a finite charge density in the trivial phase IV. But owing to the absence of a compact domain wall of the polarity density, the net topological winding number vanishes. Hence, phase IV corresponds to a quasiuniform ferromagnetic phase (or antiferromagnetic phase if $J_{||} < 0$) as seen in the untwisted CrI_3 bilayer samples [53]. Finally, large $J_\perp$ creates another compact domain wall at the center of the moiré supercell in which the topological charge is $Q = -1$.

C. Topological antiferroelectric phase

Phase II is very intriguing and requires separate discussions. The naive spin texture of this phase [Fig. 1(c)] is reminiscent of a spin spiral phase. However, unlike in the other trivial spiral phases, here several new types of topological charge centers are formed as shown in Figs. 3(l) and 4(a). First, we observe that the polarity density has a streamline flow diagram with a one-dimensional domain wall [see Fig. 3(b)]. But it fails to commence a compact geometry to produce full skyrmion charge centers. However, there exist five sharp charge centers [three inside the $n_z = -1$ (blue) region and two outside]. This structure periodically repeats in a smectic pattern. These charge centers have different origins from the previous three skyrmion phases with compact polarity density, and result from splitting of the vorticity by streamline flow of polarity density.

A zoomed-in view of the spin texture on top of the topological charge density, as shown in Fig. 4(a), unravels the mechanism of these charge centers. The charge center at the middle (blue-colored charge density) is a "meron"-like structure, but with a fractional charge of $Q \sim 2/9 \pm 0.025$. The other four charge centers form in pairs with opposite sign of charges at the moiré zone corners. The corresponding spin textures reveal that they are *antiskyrmions* [29,30], with fractional charges $Q \sim \pm 2/9 \pm 0.025$. We note that although there are five distinct meronlike charge centers with $\pm 2/9$, they are shared between neighboring moiré supercells. Apart from these concentrated point charges, another $+2/9$ (red) is spread over the moiré cell which is not clearly visible in the color map of Figs. 4(a) and 4(b). Hence, the total charge (point charge and background charge) within a given Moire supercell vanishes.

Each pair of oppositely charged antiskyrmions acts as a topological electric dipole, sitting at each lattice site of the moiré lattice. The dipole moment is estimated to be $(0.05 \pm 0.005)a$, where a is the moiré lattice constant. More interestingly, the dipoles are aligned *antiferroelectrically* between the nearest neighbors. This gives a Néel-like ordering of the topological dipole moments, in close analogy to the Néel order of magnetic moments in a honeycomb lattice.

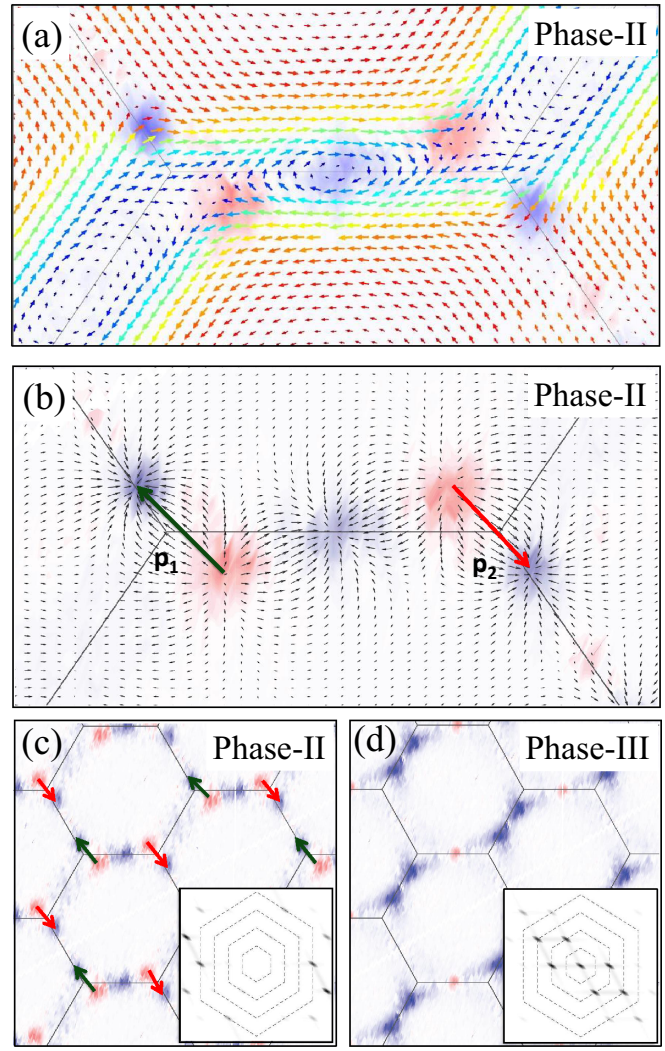

FIG. 4. Antiferroelectric phase II. (a), (b) Zoomed-in view of the topological charge density in blue to red color map plotted in the background, with arrows denoting spins **s** in (a), and emergent electric field **E** vector in (b). The spin texture clarifies the formation of topological charge at the moiré lattice side, and a pair of antiskyrmions with opposite charge centers near the moiré lattice corners. The electric field lines in (b) confirm the formation of topological dipole moment (long arrows) between the antiskyrmion pairs. (c), (d) Real space view of the topological charges in many moiré unit cells for phase II and phase III, respectively. (c) We clearly observe the Néel analog of the ordering of the topological dipole moments, giving an antiferroelectric phase. (d) As we move from phase II to phase III, the antiskyrmion pairs are annihilated and integer topological charges become confined by a compact domain wall on different lattice sides. Inset: The structure factor of the corresponding topological charge density, showing no charge ordering in phase II, as opposed to Bragg peaks in phase III.

Comparisons of the spin textures between phase II (antiferroelectric) and phase III (skyrmions) throw light on the phase transition between them. The phase transition occurs

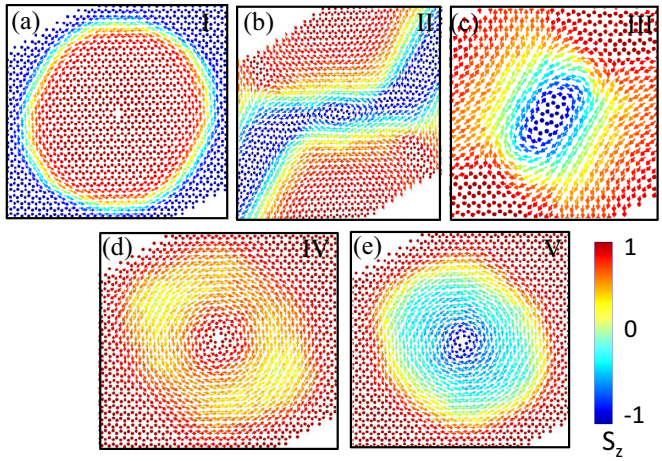

FIG. 5. Zoomed views of the spin structure in five different phases.

when the antiskyrmion pairs coalesce. This also results in the closing of the streamline flow of the polarity density to form a compact domain wall [see Fig. 3(c)]. Hence a topological winding number description becomes appropriate in phase III.

D. Electromagnetic duality

To visualize the formation of the dipole moment in phase II, we write down a gauge-dual theory, and calculate the topological electric field lines. In an electronic quantum Hall analog, we know that a physical charge is attached to a magnetic flux via the Chern-Simons coupling—also known as the Stréda formula [66]. Using this analogy, we affix an emergent gauge field $a_\mu = (\phi, \mathbf{a})$ with the topological charge density ρ as $\mathcal{J}_\mu = \epsilon_{\mu\nu\tau}\mathcal{F}_{\nu\tau}$. Here $\mathcal{F}_{\nu\tau} = \partial_\nu a_\tau$ is the corresponding curvature field tensor (an emergent electromagnetic field, but not the same $\mathbf{B}$ field seen by local spins). The emergent "electric field" is read as $\mathbf{E} = -\nabla\phi - \partial_t \mathbf{a}$. This electric field follows the Gauss law, and acquires distinct spatial dependence according to the topological charge distributions. Using the Gauss law, the electric field lines can be found numerically from $\int \mathbf{E}.d\mathbf{S} = \rho$. The electric field lines shown by black arrows in Fig. 4(b) confirm the existence of the dipole moment and their antiferroelectric ordering. We extend the calculations of electric field lines to all the other phases, and find that the field line configurations are consistent with the ring-, rod-, and pointlike charge centers as obtained in phase I, phase II, and phase V, respectively (see Fig. 9).

E. Topological correlation function

In what follows, the topological dipole moment indeed provides a measure of the order parameter in phase II: It continuously disappears in going from phase II to phase III. To elucidate this further, we compare larger views of the moiré lattice in phase II and phase III in Figs. 4(c) and 4(d). We also calculate the topological charge susceptibility as $\chi_c(\mathbf{r}) = \int d^2\mathbf{r}'\rho(\mathbf{r}')\rho(\mathbf{r}+\mathbf{r}')$. The corresponding Fourier transformation gives the structure factor $S_c(\mathbf{q})$, which mimics the XRD pattern as seen by transmission electron microscopy (TEM), and may be indirectly probed by Lorentz TEM [21]. The corresponding structure factors are plotted in the *inset* figures to Figs. 4(c) and 4(d). As expected, we observe Bragg peaks in phase III as the topological charges form a triangular lattice. The lattice also features a broken spatial rotation symmetry, and gives a smecticlike skyrmion lattice. In phase II the charge centers do not exhibit any Bragg peak up to the third Brillouin zone. As the appearance of the new Bragg-like peaks at the antiferromagnetic wave vector in the spin-spin correlation function indicates an antiferromagnetic order, similar Bragg peaks in the dipole-dipole correlation function indicate an antiferroelectric ordering of the topological dipole moments.

IV. DISCUSSIONS AND CONCLUSIONS

So far, our discussions were primarily devoted to delineate the mechanism of skyrmion charges and antiskyrmion dipoles. Although not our primary focus here, it is worthwhile to outline a few possible mechanisms to destroy topological configurations, and the corresponding phase transitions. We discussed that the size of the compact domain wall (r_d) as it reduces to zero or expands all the way to the moiré lattice vector as a function of $J_\perp/J_D$ and bilayer thickness d destroys the skyrmion configuration. Moreover, energy makes another dominant factor to destabilizing the saddle-point minima of skyrmions. Once fluctuations are included, the topological charge centers oscillate, creating "phonon"-like excitations, which melt the skyrmion crystals [67]. We have studied the short-range (nearest-neighbor) topological charge correlation function, and find that it exhibits a similar divergence behavior at all phase transition points (see Appendix C). In addition, we observe that the phase transition from phase II to phase III occurs via the coalescence of the antiskyrmion pairs and vanishing dipole moment. This is reminiscent of the Kosterlitz-Thouless (KT) like transition, but generalized to the $O(3)$ field.

Can we probe the topological electric field, dipole moment, and KT transition of the topological charge of the skyrmions? The electric field is the mediator of the force between two charge particles. Since a skyrmion charge is a topological charge, it cannot be destroyed without deforming all the spins in a skyrmion. This prohibits two skyrmions of the same charge to come close to each other—as if they experience a Coulomb repulsion between them. This phenomenon can be associated with an electric field. Much like how we measure an electric field by adding a test charge, here one can think of adding a test skyrmion in a skyrmion background, and study its dynamics. It will be found that the test skyrmion of same (opposite) charge will be repelled (attracted) from the skyrmion background. Similarly, when two skyrmions/antiskyrmions of opposite charges are spatially separated as in phase II, one can associate a dipole moment in the usual way. With tuning, the two opposite charges can either annihilate each other or the two charges can become unbound from each other. The second phenomenon is analogous to the KT transition as seen in the vortex case. In the case of the KT transition in vortices, pairs of vortices of opposite charges are energetically favorable at low temperature, which forms a dipole moment, and the material behaves as a dielectric. With increasing temperature, the vortex pairs split and the vortex charges become unbound, giving a plasmalike phase. The phase transition between them is denoted by the

KT transition. In our present case, we can speculate that a similar splitting of the dipole may occur with increasing temperature in phase II, giving us a unique opportunity to explore a possible KT transition of skyrmions.

Finally, the spin-spin correlation also plays an important role. We have calculated the transverse and longitudinal spin-spin correlation functions in the static limit. The transverse component does not have any $q \sim 0$ mode, and remains nearly unchanged across all the phases. The longitudinal susceptibility shows Bragg peaks in four phases, but not in phase I, because phase I is nonmagnetic. These additional results and discussions are given in Appendix.

One may wonder how sensitive is the phase diagram to DMI and SOC terms. We have checked that DMI brings in very little change to the spin configurations, and their topological properties are robust as long as the DMI strength is considerably weaker than $J_\perp$ and J_D. With an eye to synthesize twisted bilayers of VDW magnets [61,62], it is known that the spins are local in nature, and the materials are charge insulators. Thus the SOC does not play an important role to the skyrmion configurations.

ACKNOWLEDGMENTS

S.R. thanks Sibaram Ruidas for helps with the Monte Carlo formulation. We are thankful to the S.E.R.C. computational facility at the Indian Institute of Science. T.D. acknowledges research funding from the Department of Science and Technology, India, under the N.S.M Grant No. DST/NSM/R&D_HPC_Applications/2021/39.

APPENDIX A: EFFECTIVE INTERLAYER MAGNETIC FIELD

As mentioned in the main text, the effect of $H_{\rm ex}$ and H_D can be described by effective magnetic field $\mathbf{B}(\mathbf{r}_i)$ coming from exchange $[\mathbf{B}_{\rm ex}(\mathbf{r}_i)]$ and dipole $[\mathbf{B}_D(\mathbf{r}_i)]$. Taking all the bottom layer's spin $\mathbf{S}$ to be along the $+z$ direction, we can explicitly write the field components as

$$\mathbf{B}_{\rm ex}(\mathbf{r}_i) = J_\perp \sum_{a=1,2,3} \cos(\mathbf{G}_a.\mathbf{r}_i)\hat{\mathbf{z}}, \tag{A1}$$

$$\mathbf{B}_D(\mathbf{r}_i) = \sum_j \frac{J_D}{r_{ij}^3}\left[1 - \frac{3d^2}{r_{ij}^2}\right]\hat{\mathbf{z}} - \frac{3J_D d}{r_{ij}^5}[(x_i - x_j)\hat{\mathbf{x}} + (y_i - y_j)\hat{\mathbf{y}}]. \tag{A2}$$

The index i denotes a top layer spin. The sum over j denotes a sum over bottom layer spins and is restricted up to $r_{\rm cut} = N_{\rm cut}a_0$. Due to the higher power of r_{ij} in the denominator, it is easy to check that the summation converges very rapidly ($\approx N_{\rm cut} < 20$), much before the moiré supercell lattice vector $R_{1,2} \sim 35a_0$. $\mathbf{G}_a$ denotes the three lowest moiré reciprocal lattice vectors, d is the interlayer distance, and x_i and y_i are x and y coordinates of ith spin. $\mathbf{B}_{\rm ex}$ is plotted in Figs. 6(a) and 6(c) for $J_\perp < 0$ (ferromagnetic) and $J_\perp > 0$ (antiferromagnetic), respectively.

Clearly, a compact domain wall forms at the nodal contour of $s_z(\mathbf{r})$ where the total magnetic field roughly vanishes, i.e., $B_z(\mathbf{r}_{\rm d}) = 0$. [This approximation works better where the in-plane spin exchange $J_{||} \ll |B|$, so that the second term in Eq. (4) dominates.] Then the condition simplifies to

$$\frac{J_\perp}{J_D}\beta_{\rm ex}(\mathbf{r}_d) + \beta_D(\mathbf{r}_d) = 0, \tag{A3}$$

where $\mathbf{r}_d$ is the loci of the domain wall boundary and $\beta_{\rm ex}$ and β_D are given by

$$\beta_{\rm ex}(\mathbf{r}_d) = \sum_a \cos(\mathbf{G}_a \cdot \mathbf{r}_d), \tag{A4}$$

$$\beta_D(\mathbf{r}_d) = \sum_j \frac{1}{|\mathbf{r}_d - \mathbf{r}_j|^3}\left[1 - \frac{3d^2}{|\mathbf{r}_d - \mathbf{r}_j|^2}\right]. \tag{A5}$$

It is not easy to find an analytical expression for this nodal contour from Eqs. (A1) and (A2), but it is clear that the value of $\mathbf{r}_d$ depends on the $J_\perp/J_D$ ratio and the bilayer thickness d for a given moiré lattice denoted by $\mathbf{G}$. The equation of the nodal line can be a circle or an ellipse depending on these parameters. As we see from the numerical simulation, the domain wall is circular for large values of $J_\perp$, while it takes an elliptical form in phase III for small values of $J_\perp$.

Again in the limit of $J_{||} << |B|$, a phase transition is defined at $J_\perp/J_D = -\beta_D(\mathbf{r}_d)/\beta_{\rm ex}(\mathbf{r}_d)$ [from Eq. (A3)] for different values of $\mathbf{r}_d$. In phase I, the radius of the circular patch increases as $J_\perp \to 0$, and at the transition point to phase II two circular regions merge together at $\mathbf{r}_d = \mathbf{R}_1/2$. On the other hand, $\mathbf{r}_d$ decreases in phase V as $J_\perp \to 0$, which implies $\mathbf{r}_d = 0$ at the transition from the phase V to phase IV. Similarly transitions from phase II to III and III to IV are given by $\mathbf{r}_d = \mathbf{R}_2/2$ and $(\mathbf{R}_1 + \mathbf{R}_2)/2$, respectively. By numerically evaluating $\beta_{\rm ex}$ and β_D at various $\mathbf{r}_d$, we extract the approximate critical value of the ratio $J_\perp/J_D$ for different transitions, which are listed in Table I.

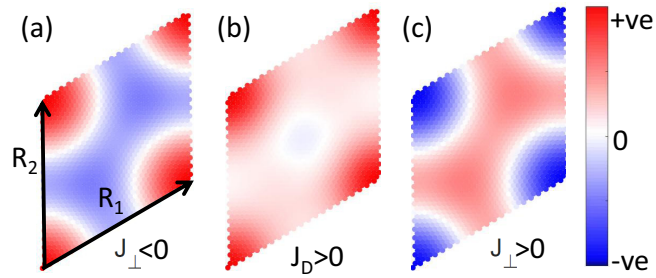

FIG. 6. Effective magnetic fields along the z direction in the moiré unit cell. (a), (c) Field due to the interlayer exchange interaction ($B_{\rm ex}$) (a) for $J_\perp < 0$ and (c) for $J_\perp > 0$. (b) Field due to the interlayer dipole interaction (B_D) for $J_D > 0$. $\mathbf{R}_1$ and $\mathbf{R}_2$ denote the two translation lattice vectors.

TABLE I. Critical values of $\mathbf{r}_d$ and $J_\perp/J_D$ at different phase transition points.

Transitions	$\mathbf{r}_d$	$J_\perp/J_D$
Phase I to phase II	$\mathbf{R}_1/2$	−0.57
Phase II to phase III	$\mathbf{R}_2/2$	−0.4
Phase III to phase IV	$(\mathbf{R}_1 + \mathbf{R}_2)/2$	0.3
Phase IV to phase V	$\mathbf{0}$	1.6

A direct comparison of transition from phase I to II and phase IV to V reveals that $|J_\perp/J_D|$ is larger on the positive side (1.6 on the positive side and -0.57 on the negative side). This can be understood from Fig. 6. At the corner of the moiré supercell $B_{\rm ex}$ and B_D have the same sign in the $J_\perp < 0$ region. So their effects add up. This is also responsible for a thin domain wall of magnetic bubbles in phase I. In the positive $J_\perp$ region, however, $B_{\rm ex}$ and B_D have opposite sign. So a larger value of $J_\perp$ is needed to overcome the effect $J_{\mathbf{D}}$ in the positive side. This leads to a wider domain wall in phase V. We should distinguish the effects of the dipole-dipole interaction H_D of the present paper compared to other studies. In earlier studies [5], such an interaction is involved for the same intralayer spin (between **s** and **s** variables) which tends to produce magnetic bubble phases [3]. On the other hand, here the dipole interaction is between the interlayer (**s** and **S**), and is detrimental to the bubble or Bloch skyrmion phases, while promoting the streamline flow of the polarity density.

APPENDIX B: DETAILS OF THE MONTE CARLO METHOD

As mentioned in the main text, the Hamiltonian for the top layer can be written as

$$H = H_1 + \sum_i \mathbf{B}(\mathbf{r}_i)\cdot\mathbf{s}_i. \tag{B1}$$

Here H_1 is the intralayer Hamiltonian and $\mathbf{B}(\mathbf{r}_i)$ is the effective magnetic field due to interlayer interaction. The lattice site $\mathbf{r_i}$ spans the moiré unit cell. In our calculation at the commensurate angle 1.61° we have 2522 basis sites per unit cell. We set all the classical spins to have unit length ($S_i = 1$) so that all the spins can be specified with two parameters S_z and ϕ where ϕ is the angle that the component of spin on the xy plane (s^{xy}) makes with the x axis. From these two parameters, we can extract all three components of the spins as

$$\begin{aligned} s_i^{xy} &= \sqrt{1-\left(s_i^z\right)^2},\\ s^x &= s^{xy}\cos(\phi),\\ s^y &= s^{xy}\sin(\phi). \end{aligned} \tag{B2}$$

We initialize the simulation with all spins pointing upward, i.e., $S_i^z = 1$, and then the next spin is chosen randomly from all the lattice points. The update algorithm for that spin is given by

$$\begin{aligned} s_i^z &= s_i^z + \gamma ds^z,\\ \phi_i &= \phi_i + \gamma d\phi. \end{aligned} \tag{B3}$$

And if $|s_i^z| > 1$ then

$$\begin{aligned} s_i^z &= 2 \mp \left(s_i^z + \gamma ds^z\right),\\ \phi_i &= \phi_i + \gamma d\phi + \pi. \end{aligned} \tag{B4}$$

Here the $\pm$ signs are for $s_i^z > 1$ and $s_i^z < -1$, respectively. γ is a random number between 1 and -1, and ds^z and $d\phi$ are ranges of s^z and ϕ.

At each Monte Carlo step we calculate the local Hamiltonian

$$H(\mathbf{r}_i)_{\rm loc} = H_1(\mathbf{r}_i) - \sum_i \mathbf{B}(\mathbf{r}_i)\cdot\mathbf{s}_i, \tag{B5}$$

$$H_1(\mathbf{r}_i) = \sum_{<i,j>} J_{||}\mathbf{s}_i\cdot\mathbf{s}_j, \tag{B6}$$

and each configuration is accepted with a Boltzmann probability $e^{[H(\mathbf{r}_i)_{\rm loc}^{\rm new} - H(\mathbf{r}_i)_{\rm loc}^{\rm old}]/k_BT}$ at temperature T. To find the low temperature Monte Carlo ground state we perform temperature annealing as well as parameter annealing, and check for convergence of the total ground state energy. We use $dS^z = 0.4$ and $d\phi = 0.4\pi$. At low temperature we decrease the value of $ds^z(=0.1)$ and $d\phi(=0.1\pi)$ to increase the acceptance ratio in Monte Carlo steps. We equilibrate the system with 10^8 steps and take the low energy configuration for another 10^8 steps.

APPENDIX C: CORRELATION FUNCTIONS AND STRUCTURE FACTORS

From Fig. 2, it is evident that there are finite topological charge distributions even in the trivial topological phases where the polarity density n_z fails to create domain walls. Therefore, to obtain the microscopic nature of how the quantum fluctuations make it possible to form topological configurations in phase I, III, and V, we investigate the following correlation functions: topological charge susceptibility,

$$\chi_c(\mathbf{r}) = \int d^2\mathbf{r}'\rho(\mathbf{r}')\rho(\mathbf{r}+\mathbf{r}'), \tag{C1}$$

and the spin-non-flip (or skyrmion polarity) and spin-flip correlation functions

$$\begin{aligned} \chi_s^{zz}(\mathbf{r}) &= \int d^2\mathbf{r}' n_z(\mathbf{r}')n_z(\mathbf{r}+\mathbf{r}'),\\ \chi_s^{\pm}(\mathbf{r}) &= \int d^2\mathbf{r}' n_+(\mathbf{r}')n_-(\mathbf{r}+\mathbf{r}'), \end{aligned} \tag{C2}$$

where $n_\pm = n_x \pm i n_y$. The Fourier transformation of the correlation function gives the structure factor $S_{c/s}(\mathbf{q})$. For the topological charge density, the topological structure factor mimics the XRD or TEM maps, except that this is not directly measurable and indirectly it can be mapped by Lorentz TEM. The two spin structure factors are however measurable via small-angle neutron scattering experiments.

Figure 7 shows structure factors and various correlation functions for different phases. First we notice that in the nontrivial phases, the topological structure factor shows distinct Bragg peaks at $\mathbf{q} \to 0$, signifying the transnational symmetry breaking and formation of the skyrmion lattice. (When the dynamics is added, this peak will disperse away from the $\mathbf{q} = 0$ point as a typical acoustic Goldstone mode.) In the trivial phase (phase II and phase IV), there are no Bragg peaks, but some weak intensity at higher Brillouin zone of the original moiré supercell which is often observed in dilute gas or liquid phases.

The spin-non-flip and spin-flip components of the spin-structure factors have the usual behavior in a skyrmion structure, while the stark difference between phase I and phase

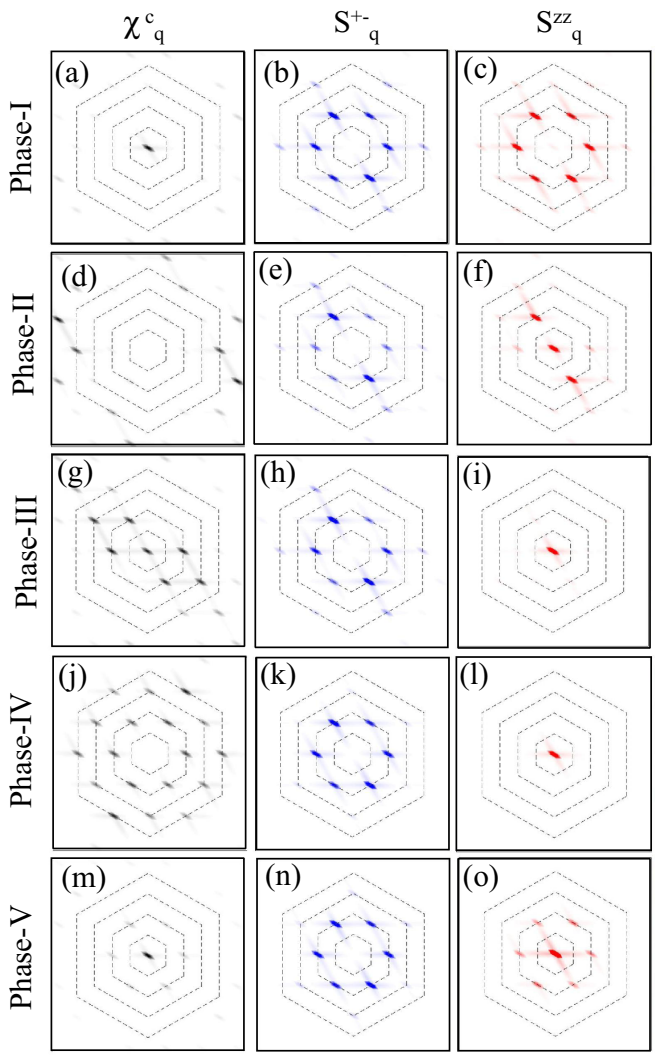

FIG. 7. Structure factors. Left: The left row gives the structure factor of the topological charge density (Fourier transformation of the charge-charge correlation function). Middle: Transverse spin-spin correlation functions. Right: Longitudinal correlation function in the momentum space. In all three cases, we give various quadrants of the Brillouin zone with dashed lines.

IV for χ_s^{zz} should be noted. In the case of a ring charge (phase I) there is no $\mathbf{q} \to 0$ mode for the polarity density since here we have a sharp domain wall boundary between the up- and down-spin states. For all other cases, the $\mathbf{q} \to 0$ mode exists, suggesting a finite value of the magnetic moment in these cases on the top layer. On the other, in phase II, the total magnetization vanishes in a moiré unit cell; however, if one defines Néel magnetization between the up-spin domain and down-spin domain, we have an antiferromagneticlike domain wall ordering. In all cases, the spin-flip structure factor is similar, while an additional spatial rotational symmetry breaking is observed in phases II and III as expected. We find that all the peaks are present in the second Brillouin zone, which is due to the fact that the Moire cell here forms a honeycomb lattice which has two sublattices.

To further elucidate the phase transition, we analyze the topological correlation function at a fixed distance ($r_i - r_j =$

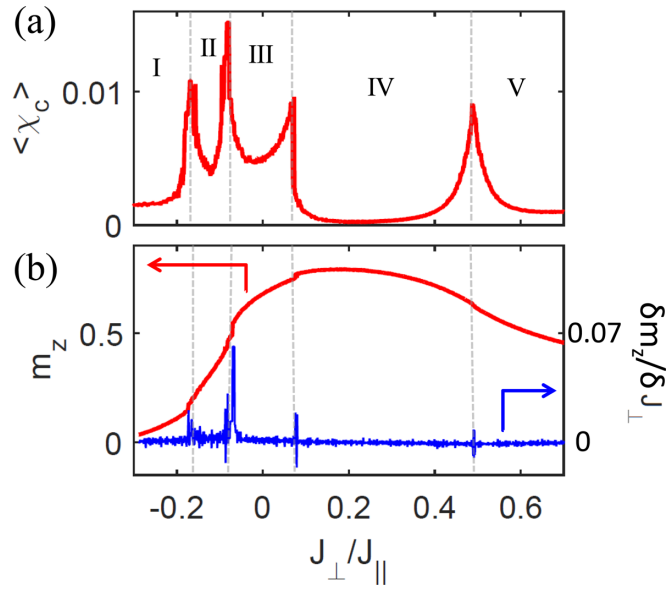

FIG. 8. (a) Average χ_c and (b) average magnetization (m_z) and derivative of m_z as a function of interlayer exchange ($J_\perp/J_{||}$) at a fixed $J_D = 0.3J_{||}$. Discontinuity in m_z at the phase transition can be seen from the jumps in derivative of m_z [blue curve in (b)].

constant):

$$\chi_c = \frac{1}{N} \sum_{<i,j>} \rho(\mathbf{r_i})\rho(\mathbf{r_j}). \tag{C3}$$

We plot the result as a function of interlayer exchange ($J_\perp$) in Fig. 8(a). This gives the short-range correlation of the topological charge density.

We find the correlation has peaks at the phase transition points as shown in Fig. 8(a). This result is consistent with jumps in the effective magnetic field $M_z = \langle (1/N) \sum_i S_i^z \rangle$ along $J_\perp$, as shown in Fig. 8(b). Near the phase transition points, the landscape of effective magnetic field changes over

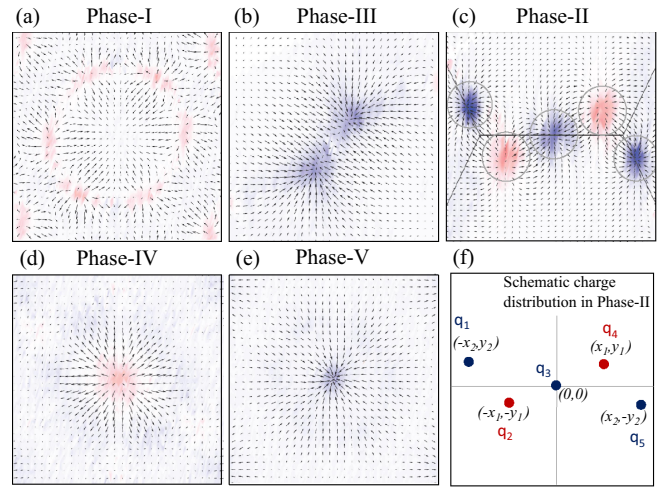

FIG. 9. (a)–(e) We have plotted the emergent topological electric field lines on top of the topological charge density in the vicinity of the charge centers (see Fig. 10 for larger view) in all five phases. In (f) we show the schematic distribution of point charges for phase II with origin of the coordinates at the charge q_3.

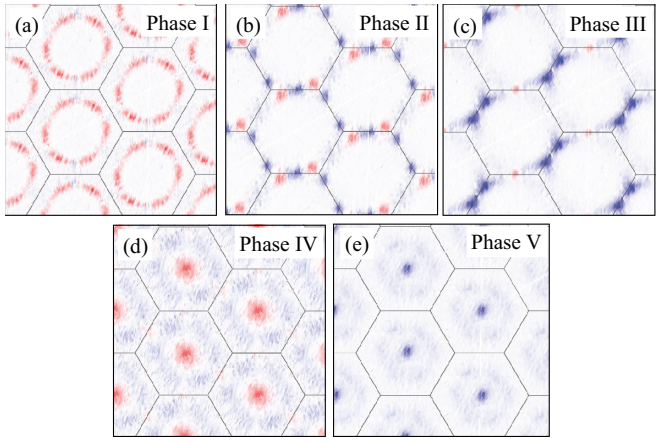

FIG. 10. Plots of topological charge density in many moiré unit cells.

the moiré unit cell. As a result near the domain wall in each phase (except phase IV where there is no domain wall) the **B** field becomes small over a large area. Therefore, the Hamiltonian is mostly dominated by strong in-plane ferromagnetic exchange ($J_{||}$), and produces a strong nearest-neighbor correlation.

We further calculate scalar chirality (not shown) $\chi_{sc} = \frac{1}{N}\langle\sum_{<i,j,k>} \mathbf{S}_i.(\mathbf{S}_j \times \mathbf{S}_k)\rangle$, where $\langle i, j, k\rangle$ denotes three spins forming the smallest triangle in the honeycomb lattice. We find that the scalar chirality vanishes in phase II and phase IV, where the magnetization has a sharp jump at their phase boundary [Fig. 8(b)].

APPENDIX D: DIPOLE AND QUADRUPOLE MOMENTS IN PHASE II

Field lines for topological charge in phase II are shown in Fig. 9(c). The field lines indicate that the charge distribution can be approximated with point charges (q_i, $i = 1, 2, 3, 4, 5$) as shown in Fig. 9(f). As the total charge of this configuration is zero we investigate the higher moments (dipole and quadrupole) of this charge distribution. We calculate the dipole moment for charge pairs (q_1, q_2) and (q_4, q_5), and taking the origin of our coordinates at one of the charge centers [see Fig. 9(f)] we calculate the quadrupole moments, which are given by

$$Q = \begin{bmatrix} Q_{xx} & Q_{xy} \\ Q_{yx} & Q_{yy} \end{bmatrix} = \begin{bmatrix} \sum_i \rho_i x_i x_i & \sum_i \rho_i x_i y_i \\ \sum_i \rho_i y_i x_i & \sum_i \rho_i y_i y_i \end{bmatrix}. \quad \text{(D1)}$$

Values of the dipole and quadrupole moments for phase II are given in Table II.

We caution the reader that the estimate of the fractional charge is subjected to the integration contour around each charge center, since there is no compact domain wall boundary here.

TABLE II. Values of charge, dipole moments, quadrupole moments in the phase II for two different dipole coupling strengths (J_D). (x,y) are given in unit of moire lattice constant $35.6a_0$.

Quantities	$J_D = 0.53$	$J_D = 1.0$
q_1	−0.23	−0.23
q_2	0.22	0.22
q_3	−0.25	−0.24
q_4	0.22	0.24
q_5	−0.20	−0.22
(x_1, y_1)	(0.20, 0.07)	(0.20, 0.07)
$(x_2, -y_2)$	(0.35, −0.09)	(0.35, −0.09)
(p_{1x}, p_{1y})	(0.033, 0.035)	(0.033, 0.035)
(p_{2x}, p_{2y})	(−0.033, −0.035)	(−0.034, −0.037)
Q_{xx}	−0.035	−0.037
Q_{yy}	−0.001	−0.001
Q_{xy}	0.021	0.020

[1] T. H. R. Skyrme, A non-linear field theory, Proc. R. Soc. A **260**, 127 (1961); A unified field theory of mesons and baryons, Nucl. Phys. **31**, 556 (1962).

[2] A. N. Bogdanov and A. Hubert, Sov. Phys. JETP **68**, 101 (1989); J. Magn. Magn. Mater. **138**, 255 (1994); U. K. Roessler, A. N. Bogdanov, and C. Pfleiderer, Nature (London) **442**, 797 (2006).

[3] N. Nagaosa and Y. Tokura, Nat. Nanotechnol. **8**, 899 (2013).

[4] J. H. Han, *Skyrmions in Condensed Matter*, Springer Tracts in Modern Physics Vol. 278 (Springer, New York, 2017).

[5] Y. S. Lin, J. Grundy, and E. A. Giess, Appl. Phys. Lett. **23**, 485 (1973); A. P. Malozemoff and J. C. Slonczewski, *Magnetic Domain Walls in Bubble Materials* (Academic, New York, 1979), pp. 306–314; T. Garel and S. Doniach, Phys. Rev. B **26**, 325 (1982); T. Suzuki, J. Magn. Magn. Mater. **31-34**, 1009 (1983); B. Göbel, J. Henk, and I. Mertig, Sci. Reports **9**, 9521 (2019); M. Ezawa, Phys. Rev. Lett. **105**, 197202 (2010).

[6] S. Rohart and A. Thiaville, Phys. Rev. B **88**, 184422 (2013).

[7] M. Hoffmann, B. Zimmermann, G. P. Muller, D. Schurhoff, N. S. Kiselev, C. Melcher, and S. Blugel, Nat. Comm. **8**, 308 (2017).

[8] E. Y. Vedmedenko, P. Riego, J. A. Arregi, and A. Berger, Phys. Rev. Lett. **122**, 257202 (2019).

[9] B. Dupé, G. Bihlmayer, M. Böttcher, S. Blügel, and S. Heinze, Nat. Commun. **7**, 11779 (2016).

[10] T. Okubo, S. Chung, and H. Kawamura, Phys. Rev. Lett. **108**, 017206 (2012).

[11] A. O. Leonov and M. Mostovoy, Nat. Commun. **6**, 8275 (2015).

[12] C. D. Batista, S. Z. Lin, S. Hayami, and Y. Kamiya, Rep. Prog. Phys. **79**, 084504 (2016).

[13] S. Hayami, S.-Z. Lin, and C. D. Batista, Phys. Rev. B **93**, 184413 (2016).

[14] S. Banerjee, O. Erten, and M. Randeria, Nat. Phys. **9**, 626 (2013).

[15] R. Ozawa, S. Hayami, and Y. Motome, Phys. Rev. Lett. **118**, 147205 (2017).

[16] I. Gross, W. Akhtar, A. Hrabec, J. Sampaio, L. J. Martinez, S. Chouaieb, B. J. Shields, P. Maletinsky, A. Thiaville, S. Rohart, and V. Jacques, Phys. Rev. Mater. **2**, 024406 (2018).

[17] S. L. Sondhi, A. Karlhede, S. A. Kivelson, and E. H. Rezayi, Phys. Rev. B **47**, 16419 (1993).

[18] L. S. Leslie, A. Hansen, K. C. Wright, B. M. Deutsch, and N. P. Bigelow, Phys. Rev. Lett. **103**, 250401 (2009).

[19] S. Mühlbauer, B. Binz, F. Jonietz, C. Pfleiderer, A. Rosch, A. Neubauer, R. Georgii, and P. Böni, Science **323**, 915 (2009).

[20] W. Münzer, A. Neubauer, T. Adams, S. Mühlbauer, C. Franz, F. Jonietz, R. Georgii, P. Böni, B. Pedersen, M. Schmidt, A. Rosch, and C. Pfleiderer, Phys Rev. B **81**, 041203(R) (2010).

[21] X. Z. Yu, Y. Onose, N. Kanazawa, J. H. Park, J. H. Han, Y. Matsui, N. Nagaosa, and Y. Tokura, Nature (London) **465**, 901 (2010); D. Morikawa, K. Shibata, N. Kanazawa, X. Z. Yu, and Y. Tokura, Phys. Rev. B **88**, 024408 (2013).

[22] P. Milde, D. Köhler, J. Seidel, L. M. Eng, A. Bauer, A. Chacon, J. Kindervater, S. Mühlbauer, C. Pfleiderer, S. Buhrandt, C. Schütte, and A. Rosch, Science **340**, 1076 (2013).

[23] S. Seki, X. Z. Yu, S. Ishiwata, and Y. Tokura, Science **336**, 198 (2012).

[24] Y. Tokunaga, X. Z. Yu, J. S. White, H. M. Ronnow, D. Morikawa, Y. Taguchi, and Y. Tokura, Nat. Commun. **6**, 7638 (2015).

[25] X. Zhao, C. Jin, C. Wang, H. Du, J. Zang, M. Tian, R. Che, and Y. Zhang, Proc. Natl. Acad. Sci. USA **113**, 4918 (2016).

[26] S. Heinze, K. von Bergmann, M. Menzel, J. Brede, A. Kubetzka, R. Wiesendanger, G. Bihlmayer, and S. Blügel, Nat. Phys. **7**, 713 (2011).

[27] Z. Hou, W. Ren, B. Ding, G. Xu, Y. Wang, B. Yang, Q. Zhang, Y. Zhang, E. Liu, F. Xu, W. Wang, G. Wu, X.-X. Zhang, B. Shen, and Z. Zhang, Adv. Mater. **29**, 1701144 (2017).

[28] R. Wiesendanger, Nanoscale magnetic skyrmions in metallic films and multilayers: A new twist for spintronics, Nat. Rev. Mat. **1**, 16044 (2016).

[29] A. K. Nayak, V. Kumar, T. Ma, P. Werner, E. Pippel, R. Sahoo, F. Damay, U. K. Rüßler, C. Felser, and S. S. P. Parkin, Nature (London) **548**, 561 (2017).

[30] W. Koshibae and N. Nagaosa, Nat. Commun. **7**, 10542 (2016).

[31] N. Romming, C. Hanneken, M. Menzel, J. E. Bickel, B. Wolter, K. von Bergmann, A. Kubetzka, and R. Wiesendanger, Science **341**, 636 (2013).

[32] J. Sampaio, V. Cros, S. Rohart, A. Thiaville, and A. Fert, Nat. Nanotechnol. **8**, 839 (2013).

[33] M. Mochizuki, X. Z. Yu, S. Seki, N. Kanazawa, W. Koshibae, J. Zang, M. Mostovoy, Y. Tokura, and N. Nagaosa, Nat. Mater. **13**, 241 (2014).

[34] W. Jiang, P. Upadhyaya, W. Zhang, G. Yu, M. B. Jungfleisch, F. Y. Fradin, J. E. Pearson, Y. Tserkovnyak, K. L. Wang, O. Heinonen, S. G. E. te Velthuis, and A. Hoffmann, Science **349**, 283 (2015).

[35] A. Fert, N. Reyren, and V. Cros, Nat. Rev. Mater. **2**, 17031 (2017); A. Fert, V. Cros, and J. Sampaio, Skyrmions on the track, Nat. Nanotechnol. **8**, 152 (2013).

[36] S. S. P. Parkin, M. Hayashi, and L. Thomas, Science **320**, 190 (2008).

[37] R. Tomasello, E. Martinez, R. Zivieri, L. Torres, M. Carpentieri, and G. Finocchio, Sci. Rep. **4**, 6784 (2014); P. F. Bessarab, G. P. Müller, I. S. Lobanov, F. N. Rybakov, N. S. Kiselev, H. Jónsson, V. M. Uzdin, S. Blügel, L. Bergqvist, and A. Delin, Sci. Reports **8**, 3433 (2018).

[38] X. Wang, K. Du, Y. Y. F. Liu, P. Hu, J. Zhang, Q. Zhang, M. H. S. Owen, X. Lu, C. K. Gan, and P. Sengupta, 2D Materials **3**, 031009 (2016).

[39] J. U. Lee, S. Lee, J. H. Ryoo, S. Kang, T. Y. Kim, P. Kim, C. H. Park, J. G. Park, and H. Cheong, Nano Lett. **16**, 7433 (2016).

[40] P. A. Joy and S. Vasudevan, Phys. Rev. B **46**, 5425 (1992).

[41] C. C. Mayorga-Martinez, Z. Sofer, D. Sedmidubsky, S. Huber, A. Y. S. Eng, and M. Pumera, ACS Appl. Mater. Interfaces **9**, 12563 (2017).

[42] Z. Fei, B. Huang, P. Malinowski, W. Wang, T. Song, J. Sanchez, W. Yao, D. Xiao, X. Zhu, A. F. May, W. Wu, D. H. Cobden, J.-H. Chu, and X. Xu, Nat. Mater. **17**, 778 (2018).

[43] H. J. Deiseroth, K. Aleksandrov, C. Reiner, L. Kienle, and R. K. Kreme, Eur. J. Inorg. Chem. **2006**, 1561 (2006).

[44] M. Kan, S. Adhikari, and Q. Sun, Phys. Chem. Chem. Phys. **16**, 4990 (2016).

[45] C. Ataca, H. Şahin, and S. Stable, J. Phys. Chem. C **116**, 8983 (2012).

[46] Y. Ma, Y. Dai, M. Guo, C. Niu, Y. Zhu, and B. Huang, ACS Nano **6**, 1695 (2013).

[47] M. Bonilla, S. Kolekar, Y. Ma, H. C. Diaz, V. Kalappattil, R. Das, T. Eggers, H. R. Gutierrez, M.-H. Phan, and M. Batzill, Nat. Nanotechnology **13**, 289 (2018).

[48] G. Duvjir, B. K. Choi, I. Jang, S. Ulstrup, S. Kang, T. T. Ly, S. Kim, Y. H. Choi, C. Jozwiak, A. Bostwick, E. Rotenberg, J.-G. Park, R. Sankar, K.-S. Kim, J. Kim, and Y. Jun Chang, Nano. Lett. **18**, 5432 (2018).

[49] C. Gong, L. Li, Z. Li, H. Ji, A. Stern, Y. Xia, T. Cao, W. Bao, C. Wang, Y. Wang, Z. Q. Qiu, R. J. Cava, S. G. Louie, J. Xia, and X. Zhang, Nature (London) **546**, 265 (2017).

[50] B. Huang, G. Clark, E. N. Moratalla, D. R. Klein, R. Cheng, K. L. Seyler, D. Zhong, E. Schmidgall, M. A. McGuire, D. H. Cobden, W. Yao, D. Xiao, P. J. Herrero, and X. Xu, Nature (London) **546**, 270 (2017).

[51] B. Huang, G. Clark, D. R. Klein, D. MacNeill, E. N. Moratalla, K. L. Seyler, N. Wilson, M. A. McGuire, D. H. Cobden, D. Xiao, W. Yao, P. J. Herrero, and X. Xu, Nat. Nanotechnology **13**, 544 (2018).

[52] S. Jiang, L. Li, Z. Wang, K. F. Mak, and J. Shan, Nat. Nanotechnology **13**, 549 (2018).

[53] N. Sivadas, S. Okamoto, X. Xu, C. J. Fennie, and D. Xiao, Nano Lett. **18**, 7658 (2018).

[54] K. Hejazi, Z.-X. Luo, and L. Balents, Proc. Natl. Acad. Sci. USA **117**, 10721 (2020).

[55] T. Bömerich, L. Heinen, and A. Rosch, Phys. Rev. B **102**, 100408(R) (2020).

[56] Q. Tong, F. Liu, J. Xiao, and W. Yao, Nano Lett. **18**, 7194 (2018).

[57] M. Akram and O. Erten, Phys. Rev. B **103**, L140406 (2021).

[58] M. Yang, Q. Li, R. V. Chopdekar, R. Dhall, J. Turner, J. D. Carlström, C. Ophus, C. Klewe, P. Shafer, A. T. N'Diaye, J. W. Choi, G. Chen, Y. Z. Yu, C. Hwang, F. Wang, and Z. Q. Qiu, Science Advances **6**, eabb5157 (2020).

[59] T.-E. Park, L. Peng, J. Liang, A. Hallal, F. S. Yasin, X. Zhang, K. M. Song, S. J. Kim, K. Kim, M. Weigand, G. Schutz, S. Finizio, J. Raabe, K. Garcia, J. Xia, Y. Zhou, M. Ezawa, X. Liu, J. Chang, H. C. Koo *et al.* Phys. Rev. B **103**, 104410 (2021).

[60] T. Bömerich, L. Heinen, and A. Rosch, arXiv:2004.13684 v2.
[61] M. A. McGuire, H. Dixit, V. R. Cooper, and B. C. Sales, Chem. Mater. **27**, 612 (2015).
[62] D. J. ÓHara, T. Zhu, A. H. Trout, A. S. Ahmed, Y. K. Luo, C. H. Lee, M. R. Brenner, S. Rajan, J. A. Gupta, D. W. McComb, and R. K. Kawakami, Nano Lett. **18**, 3125 (2018).
[63] A. Bansil, H. Lin, and T. Das, Rev. Mod. Phys. **88**, 021004 (2016); M. Z. Hasan and C. L. Kane, **82**, 3045 (2010); X. L. Qi and S. C. Zhang, **83**, 1057 (2011).
[64] A. Malozemoff, and J. Slonczewski, *Magnetic Domain Walls in Bubble Materials* (Academic, New York, 1979); A. H. Eschenfelder, *Magnetic Bubble Technology* (Springer-Verlag, Berlin, 1980).
[65] T. Bzdušek, Q. Wu, A. Rüegg, M. Sigrist, and A. A. Soluyanov, Nature (London) **538**, 75 (2016).
[66] P. Streda, J. Phys. C **15**, L717 (1982).
[67] P. Huang, T. Schönenberger, M. Cantoni, L. Heinen, A. Magrez, A. Rosch, F. Carbone, and H. M. Ronnow, Nat. Nanotech. **15**, 761 (2020).